3D cyclorama for digital unrolling and visualisation of deformed tubes

Authors: Charalambos Rossides[1,2], Sylvia L. F. Pender[2,3], Philipp Schneider*[1,4]

Affiliations:

[1]Bioengineering Science Research Group, Faculty of Engineering and Physical Sciences, University of Southampton, Southampton, UK

[2]School of Clinical and Experimental Sciences, Faculty of Medicine, University of Southampton, Southampton, UK

[3]Institute for Life Sciences, University of Southampton, Southampton, UK

[4]High-Performance Vision Systems, Center for Vision, Automation & Control, AIT Austrian Institute of Technology, Vienna, Austria

Emails:

Charalambos Rossides, MSc   c.rossides@soton.ac.uk

Sylvia Pender, PhD   s.pender@soton.ac.uk

Philipp Schneider, PhD   p.schneider@soton.ac.uk

*Corresponding author:

Philipp Schneider

University of Southampton

Highfield Campus

Building 7 (Lanchester) / Room 4031 – Mailpoint M7

SO17 1BJ, Southampton, UK

Email: p.schneider@soton.ac.uk

Number of words:

Abstract = 196

Manuscript = 4748 (Introduction, Validation of the 3D cyclorama method, Discussion,

Conclusion)

Number of figures:

Colour = 4

Black & white = 1

Number of supplementary figures:

Colour = 6

Black & white = 0

Number of supplementary videos:

Colour = 0

Black & white = 3

Disclosures:

All authors state that they have no conflicts of interest.

Abstract

Colonic crypts are tubular glands that multiply through a symmetric branching process called crypt fission. During the early stages of colorectal cancer, the normal fission process is disturbed, leading to asymmetrical branching or budding. The challenging shapes of the budding crypts make it difficult to prepare paraffin sections for conventional histology, resulting in colonic cross sections with crypts that are only partially visible. To study crypt budding *in situ* and in 3D, we employ X-ray micro-computed tomography to image intact colons, and a new method we developed (3D cyclorama) to digitally unroll them. Here, we present, verify and validate our '3D cyclorama' method that digitally unrolls deformed tubes of non-uniform thickness. It employs principles from electrostatics to reform the tube into a series of onion-like surfaces, which are mapped onto planar panoramic views. This enables the study of features extending over several layers of the tube's depth, demonstrated here by two case studies: (i) microvilli in the human placenta and (ii) 3D-printed adhesive films for drug delivery. Our 3D cyclorama method can provide novel insights into a wide spectrum of applications where digital unrolling or flattening is necessary, including long bones, teeth roots and ancient scrolls.

Keywords

Colorectal cancer, Crypt branching, Computed tomography (CT), 3D cyclorama, Digital unrolling, Digital flattening, Digital straightening.

1.   Introduction

In health, crypts or colonic crypts, which are tubular glands in the colon [1] (see Figure 1), multiply through a symmetric branching process called 'crypt fission'. The process begins with a single parent crypt that splits into two identical daughters [2,3]. During the early developmental stages of colorectal cancer (CRC), the fission process is disturbed [2,4,5]. This leads to asymmetrical branching or budding, where the splitting process does not complete, and the daughter crypt remains attached to its parent. Standard practice in CRC research involves the use of animal models, where animals are killed and their colon excised. Small tissue samples of the colon are typically isolated, cut open longitudinally and flattened before being embedded in wax blocks to examine the morphological changes of colonic crypts [6-9]. Paraffin physical sections of the physically flattened and embedded colons may then be taken parallel to the colonic mucosa [10] to study the shapes of the crypt cross sections (see Figure 1). Conversely, when it is necessary to capture the entire crypt on a microscope slide, e.g. to study crypt budding, the physical sections of the colon need to be taken along individual crypts, i.e. perpendicular to the colonic mucosa and across different tissue layers [11,12]. In the specific case where the morphology of crypt budding is of interest, the challenging shapes of the crypts make it difficult to (routinely) prepare such sections along individual crypts, resulting in colonic cross sections with crypts that are only partially visible (see Figure 1). Traditionally, this involves turning the murine colon into a Swiss roll, a technique whereby the entire intestine (6-7 cm in length) is cut longitudinally, laid flat, then rolled into a spiral before chemical fixation and paraffin embedding [13]. After this procedure, the distal colon is then usually located at the centre, whilst the proximal colon at the outside of the roll. 2D cross-sectional cut sections of the roll allow for histological studies of morphological abnormalities or any other tissue features over the whole length of the rodent colon using conventional light microscopy.
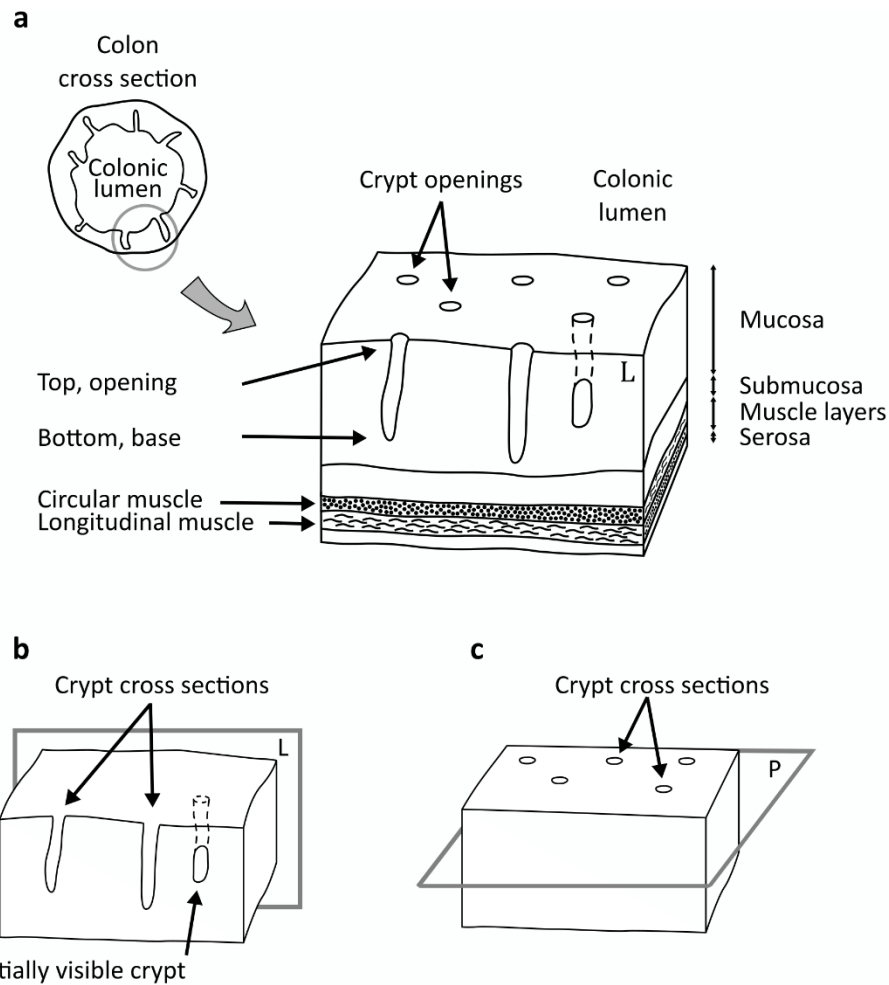
Figure 1: Colonic histology

3D schematics of the tissue layers in a healthy colon. (a) The colon is composed of four main layers: mucosa, submucosa, muscle layers and serosa. The mucosa is the layer closer to the colonic lumen, and it is comprised by a pattern of colonic crypts (tubular glands). (b) The crypts have elongated shapes in a cross-sectional view, corresponding to plane 'L' (crypts cut longitudinally). Crypts that are cut at an angle by a sectioning plane are only partially visible. (c) The crypts have rounded shapes in a cross-sectional view corresponding to plane 'P' (perpendicular to the elongated crypts).

X-ray computed tomography (CT) has been introduced as a three-dimensional (3D) clinical imaging technique in the 1970s. In the decades that followed, improvements in the attainable spatial resolution [14] have been achieved and X-ray micro-computed tomographic (μCT) volumetric imaging has been developed to non-destructively image small samples (order of cm^3 and smaller) *ex vivo*, in

53   3D, and at exceedingly higher spatial resolutions (order of μm) [15]. Using soft tissue-optimised μCT, the

54   2D nature of traditional thin-section histology can be expanded to the native 3D world ('3D X-ray

55   histology') [16]. As μCT is a 3D non-destructive imaging technique, embedded tissue samples can be

56   imaged in their original shape (deformed tubes), without any structural deformations that come along

57   with physical cutting and/or rolling into Swiss rolls, respectively. Imaging and visualising the whole

58   colonic volume in 3D by μCT is beneficial because the native shape of the colonic crypts is preserved

59   for morphological analysis. Digital unrolling of the imaged colonic volume would facilitate the

60   investigation of the tubular samples at different tissue depths, and enable identification of crypt

61   budding.

62   Apart from colons, volumes that are roughly cylindrical in shape and include features extending

63   radially through the tissue depth, are prominent in biological tissues. These include teeth roots made

64   up of layers of annual cementum growth, or the tubular shaft of long bones that contain vascular and

65   bone cell networks, for instance. We recently applied propagation based phase-contrast X-ray

66   synchrotron radiation CT (SR CT) to non-destructively image fossilised cementum increments in 3D,

67   and recorded lifespans in early mammaliaforms by counting the annual growth increments in tooth-

68   root cementum [17,18]. As cementum increments occasionally split and coalesce, 3D imaging and analysis

69   can be superior to alternative 2D techniques and methods, by avoiding errors in counts of cementum

70   layers based on the analysis of a limited number of 2D cross sections [19]. In bones, the vast bone cell

71   networks formed by osteocytes, the most abundant bone cells, are receiving increasing interest.

72   Imaging and quantifying their 3D structure [20,21] can enhance the understanding of bone development

73   in health and disease, including osteoporosis and osteoarthritis. 3D imaging approaches for both

74   tooth-root cementum and the osteocyte networks in bone would greatly benefit from a tool to

75   digitally unroll the tubular structure at hand, and represent individual tissue layers with images

76   arranged in a stack. Two further biomedical applications, namely the study of microvilli in the human

77   placenta and 3D-printed pharmaceutical films, are briefly mentioned here as they are discussed in

78   detail as case studies in section 'Supplementary'. Despite the broad range of applications and the

79   utility of a tool for digital volume unrolling, to the best knowledge of the authors, unrolling of

80   deformed objects of non-uniform thickness has not been tackled yet.

81   Here, we present a new method to digitally unroll the volume of deformed tubes of non-uniform

82   thickness, including but not confined to, colons, teeth roots, long bones, and 3D-printed

83   pharmaceutical films. Our approach reduces the problem of volumetric unrolling of deformed tubes

84   down to the simpler, and already solved problem [22-28] of mapping 3D surfaces onto planar equivalents.

85   We begin by reformulating the internal volume of the deformed tube into a series of non-intersecting,

86   equidistant, onion-like, 3D surfaces using notions from electrostatics: Virtual electrical charges are

87   applied on the tube's boundaries, and by deriving the resulting (virtual) electric field lines, we can

88   generate internal 3D surfaces that follow the shape of the deformed tube. We then apply a proof-of-

89   concept approach to map these 3D surfaces onto planar panoramic views that we call '3D cyclorama'

90   (see section '2. Methods: 3D cyclorama design and development' for a detailed description of the

91   method).

92   We verified our implementation by testing and quantifying its ability to digitally unroll an *in silico*

93   phantom we designed for this purpose (see supplementary section 'S.1. Verification of the 3D

94   cyclorama method'). We then validated our 3D cyclorama method by testing its capability to digitally

95   unroll a murine colon and identify crypt budding during early-stage CRC (see section '3. Validation of

96   the 3D cyclorama method'). Further, two biomedical case studies are presented in section

97   'Supplementary' on (i) microvilli in 'S.2 Case study: Human placenta', and on (ii) 3D-printed

98   pharmaceutical films for drug delivery in 'S.3 Case study: Pharmaceutical film'. These provide insights

99   into a wide spectrum of potential applications of the presented 3D cyclorama method to unroll

100   deformed cylindrical tubes of non-uniform thickness.

7

## 2.   Methods: 3D cyclorama design and development

2.1.   Overview

To the best of the authors' knowledge, the problem of digital unrolling of deformed tubes has not

been solved and addressed in the literature to date. However, the problem of digital unrolling of 3D

surfaces has been extensively studied, where predominant applications include straightening wrinkled

paper [22-24] and virtual unrolling of ancient papyri [25-28]. These methods usually attempt to recover text

that is written on deformed sheets by fitting 3D surfaces and digitally mapping them onto planar

images. Surface meshing (generating a set of interconnected points that represent the surface) and

image deformation are also extensively used in computer graphics for image or 3D model

representation [29-33]. These methods typically require a set of mapped points (source points mapped

to target points) to locally stretch or shrink the image or surface (non-rigid image deformation) so that

the source points match up with their targets. When it comes to volumetric image deformation, i.e.

flattening of thin sheets with uniform thickness, commercial software such as the plug-in developed

by the Konrad-Zuse-Zentrum Berlin (ZIB) [25] for Amira (Amira 6.5; ZIB/Thermo Fisher Scientific,

Germany/USA) are available. However, unrolling volumetric deformed tubes or scrolls of non-uniform

thickness adds another level of complexity. Our approach to this problem is to simplify the geometry

by reformulating the deformed tube of non-uniform thickness into a series of non-intersecting,

equidistant, onion-like 3D surfaces, which may then be mapped onto 2D (planar) equivalents via any

of the existing methods.

We first define the tube volume using the inner and outer boundary of the tube in 3D. Given an image

stack depicting the deformed cylindrical tube, these boundaries are defined as a collection of inner

and outer boundary contours drawn manually on 2D image slices. We then virtually charge the sample

boundaries with (virtual) electrical charges and simulate the field lines of the resulting electrostatic

field (see Figure 2a). This allows us to define intermediate or internal contours that are non-

intersecting and follow the shape of the sample. Each internal contour is defined at a certain

126   percentage of the local thickness of the deformed tube (see Figure 2b) so that each internal contour

127   corresponds to a relative local thickness. The internal contours are used to create internal (onion-like)

128   re-slicing surfaces. This is the point where the problem is simplified to the already solved problem of

129   mapping re-slicing surfaces onto 2D equivalents: Several approaches exist to solve this problem as

130   mentioned earlier (see also section '4. Discussion') with varying degrees of complexity. Here, we adopt

131   a simple method to non-rigidly map the re-slicing surfaces onto rectangular 2D surfaces. The 2D

132   (planar) surfaces are stacked together to provide panoramic views at different depths of the tubular

133   volume, which we call '3D cyclorama' (see Figure 3d).

134   We implemented and tested the 3D cyclorama method as a Jython script in Fiji [34] (ImageJ version

135   2.0.0-rc-68/1.52g, Java 1.8.0_66), a scientific image processing software package written in Java that

136   is distributed as an extended version of ImageJ [35,36]. Jython is an implementation of the Python

137   programming language that runs on Java platforms and is provided as one of the available scripting

138   languages in Fiji. In the following, we describe in detail the implementation and validation of our 3D

139   cyclorama method.
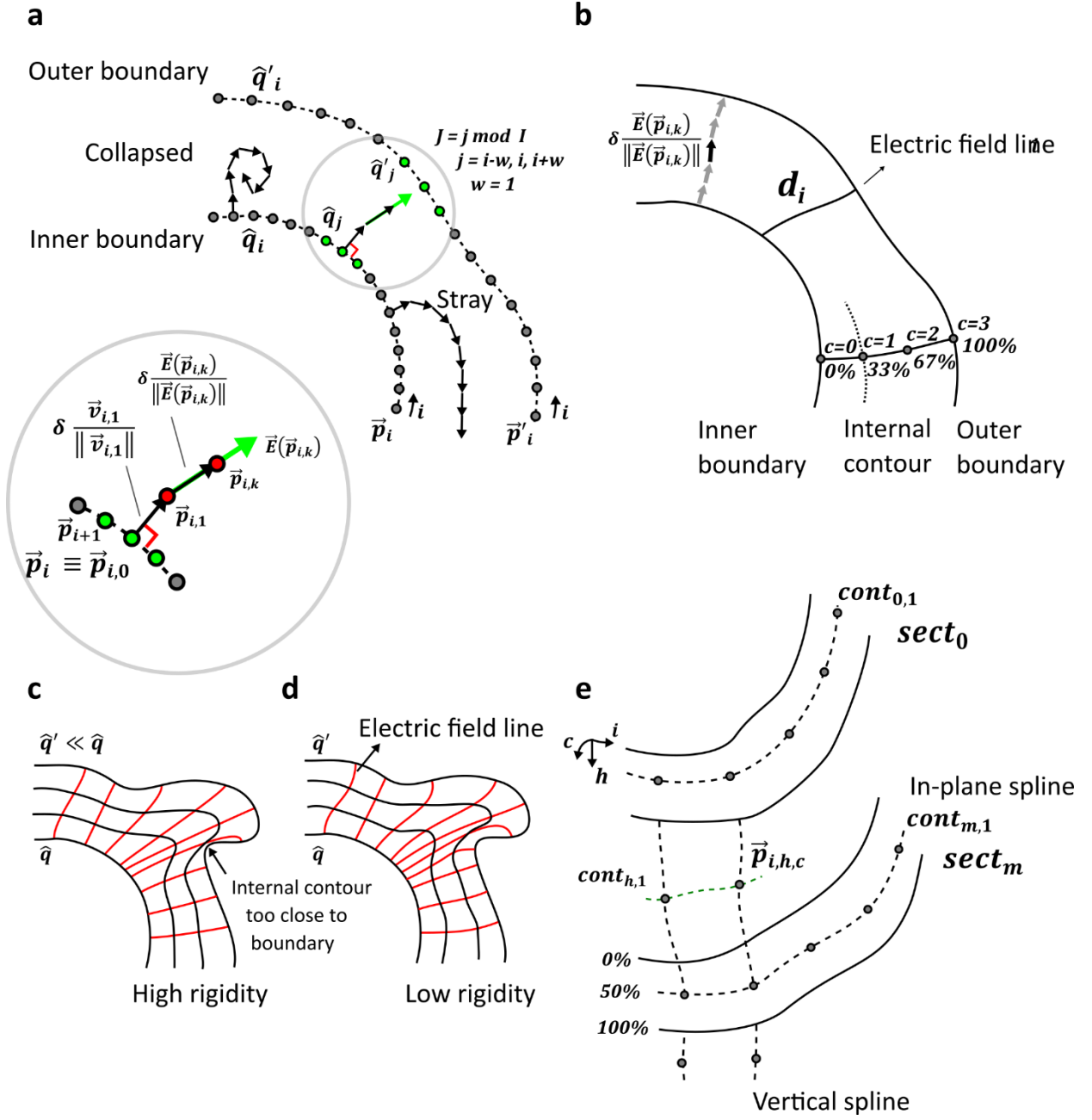
Figure 2: Generation of 3D cycloramas through electrostatic fields

(a) Boundary contours are defined on the deformed tube boundaries as sequences of charged points $\vec{p}_i$ and $\vec{p}'_i$. Each electric field line is built up incrementally starting at point $\vec{p}_i \equiv \vec{p}_{i,0}$. The first increment $\delta \cdot \frac{\vec{v}_{i,1}}{\|\vec{v}_{i,1}\|}$ is normal to the inner boundary. Each subsequent increment $\delta \cdot \frac{\vec{E}(\vec{p}_{i,k})}{\|\vec{E}(\vec{p}_{i,k})\|}$ is defined as the direction of the electric field scaled by δ (electric field line segment size), computed at the tip of the previous increment $\delta \cdot \frac{\vec{E}(\vec{p}_{i,k-1})}{\|\vec{E}(\vec{p}_{i,k-1})\|}$, considering charges on both boundaries in a user-defined

147   window (green points ⬤). This process might fail to connect point $\vec{p}_i$ to the outer boundary, resulting

148   in 'collapsed' or 'stray' lines, which are identified and removed in our cyclorama method. (b) The local

149   thickness is defined as the length d_i of field line i. Intermediate contours $cont_{h,c}$ are defined on a

150   total of C relative depth levels $\frac{c}{C-1} \cdot 100\%$ $(c = 0,1,\dots,C-1)$. (c) Stiff field lines (high *rigidity*) do not

151   properly follow the curvature of the outer boundary. (d) Lower *rigidity* results in more flexible field

152   lines, pushing the intermediate contours away from the boundaries. (e) The process shown in a-d is

153   performed on every m^{th} section of the image stack. The remaining contours $cont_{h,c}$ on sections $sect_h$

154    $(h \neq 0, m, 2m, \dots)$ are generated by fitting vertical cubic splines.

2.2. Meshing: Generation of internal contours and re-slicing surfaces

156   A sampling grid (set of onion-like surfaces) within the deformed tube is generated as a set of

157   intermediate or internal contours, corresponding to incremental relative local depth levels (0% to

158   100%) as follows: Given is a stack of images depicting 2D cross sections of a vertically aligned deformed

159   tube, for instance provided as individual reconstructed CT slices at different heights of the sample.

160   Thus, each slice represents a deformed 2D annulus that is defined by its inner and outer boundaries.

161   The boundaries are subsequently used to interpolate the enclosed cross-sectional area and describe

162   the internal contours at different relative local thickness levels.

163   We define the local thickness by employing notions from physics, namely electrostatics. Firstly, we

164   assume that the inner and outer boundaries of the cross sections are loaded by opposite electrical

165   charges. We calculate the (virtual) 2D electric field lines within the enclosed space described by those

166   boundaries as shown in Figure 2. The theory governing electrostatic fields [37] ensures that electric field

167   lines never cross and that they never form closed loops (they always start at one boundary and cross

168   the tube to reach the other boundary). Moreover, the electric field lines are always perpendicular to

169   the charged boundaries. These properties make the electric field lines an ideal tool for the definition

170   of the relative local 2D thickness, which we define here as the length d_i of the respective electric field

171   line i, spanning the inner and outer boundary of the tube's cross section (see Figure 2b).

172   The electric field $\vec{E}$ at point $\vec{p}$ is defined as the sum of the contributions from points $\vec{p}_j$ in space, each

173   charged with an electric charge q_j:

$$\vec{E}(\vec{p}) = \sum_{j=1}^{N} \frac{q_j}{4\pi\varepsilon_o} \frac{(\vec{p}-\vec{p}_j)}{\|\vec{p}-\vec{p}_j\|^3} , \tag{1}$$

174   where ε_o is the electric constant, $j = 1 \dots N$ is the set of contributing charges, and $\| \quad \|$ denotes the

175   Euclidean distance. Due to the computational costs involved to calculate the exact electric field at all

176   possible positions in space, Equation (1) was not implemented directly here, but the following

177   computational approach has been developed to approximate the electric field lines:

178   1. First, the boundary contours are defined as sequences of equidistant points $\vec{p}_i$ and $\vec{p}'_i$ ($i = 0 \dots I -$

179   1) for the inner and outer boundary, respectively, with the total number of points I being a (positive)

180   integer given by the user. These points define the positions of the electrical charges that are used for

181   the calculation of the field lines. Each point on the contour can be identified by an index i that is used

182   to select the contributing charges as discussed next (see Figure 2). Note that for tubes the boundary

183   (and internal) contours are closed, and hence the locations of the starting points $\vec{p}_{i=0}$ and $\vec{p}'_{i=0}$ are

184   arbitrary. However, it is important for the generation of cycloramas (see section '2.3. Mapping:

185   Generation of 3D cycloramas') that the sequences of points on the internal and external boundary are

186   paired, i.e., points with index i on the two opposing boundary contours are fairly close to each other.

187   This will be ensured via appropriate selection of the starting points.

188   2. Each electric field line i is built up incrementally, by starting at the location of charge q_i (point $\vec{p}_i \equiv$

189     $\vec{p}_{i,0}$ on the inner boundary contour) and computing the electric field at points $\vec{p}_{i,k}$. Due to the term

190     $\|\vec{p} - \vec{p}_j\|$ in the denominator of Equation (1) singularities may arise when point $\vec{p}$ is very close to the

191   charged points $\vec{p}_j$, as this would result in division by zero. To avoid this problem, the first calculation

192   of the electric field is bypassed and replaced by progressing along the direction of the vector $\vec{v}_{i,1}$,

193   which is perpendicular to the boundary contour at the location $\vec{p}_{i,0}$ of charge q_i, pointing inwards the

194   annulus (see Figure 2a). The vector $\vec{v}_{i,1}$ is calculated as the vector perpendicular to the tangent vector

195     $\vec{u}_i = (u_{i,x}, u_{i,y}) \coloneqq \vec{p}_{i+1,0} - \vec{p}_{i,0}$ as follows:

$$\vec{v}_{i,1} := \pm\left(u_{i,y}, -u_{i,x}\right). \tag{2}$$

196 The first step for each field line i is calculated by progressing in a straight line along the direction of

197 the vector $\vec{v}_{i,1}$ for a user-defined length δ ('electric field line segment size' in number of pixels):

$$\vec{p}_{i,1} = \vec{p}_{i,0} + \delta \, \frac{\vec{v}_{i,1}}{\|\vec{v}_{i,1}\|}. \tag{3}$$

198 Note that Equation (2) has two solutions ($\pm$), one points towards the annulus and the other points

199 away from the annulus. The correct solution is chosen by selecting the resulting point $\vec{p}_{i,1}$ that lies

200 within the annulus. Since the inner and outer boundaries are closed lines, the annulus may be defined

201 as the enclosed region. In ImageJ the contours are defined as regions of interest (ROIs) and the annulus

202 is computed as their set difference (XOR function).

203 3. As the magnitude of the electric field drops with the second power of the distance from the

204 contributing charges (see Equation (1)), we approximate the electric field at point $\vec{p}_{i,k}$ by only

205 considering charges that are close to point $\vec{p}_{i,k}$. The contributing charges are selected as the sequences

206 of points on the two boundary contours within a user-defined 'electric field search window' around

207 index i (see Figure 2a):

$$J := j \bmod I, \ j = i - w, \dots, i, \dots, i + w, \ w \in \mathbb{N}, \tag{4}$$

208 where w is a user-defined integer that defines the window size. The modulo operator mod enables

209 closing the contours by selecting points at either ends of the sequence $j = i - w, \dots, i, \dots, i + w$,

210 $w \in \mathbb{N}$, when i is too small ($i < w$) or too large ($i + w > I$). The electric field line i is built upon the

211 first computed point $\vec{p}_{i,1} = \vec{p}_{i,0} + \delta \, \frac{\vec{v}_{i,1}}{\|\vec{v}_{i,1}\|}$ as a sequence of straight electric field line segments of

212 length δ (electric field line segment size):

$$\vec{p}_{i,k} = \vec{p}_{i,k-1} + \delta \frac{\vec{E}(\vec{p}_{i,k})}{\|\vec{E}(\vec{p}_{i,k})\|}, \tag{5}$$

213 where

$$\vec{E}(\vec{p}_{i,k}) = \sum_{j \in J} \hat{q}_j \frac{(\vec{p}_{i,k} - \vec{p}_{j,0})}{\| \vec{p}_{i,k} - \vec{p}_{j,0} \|^3} + \sum_{j \in J} \hat{q}'_j \frac{(\vec{p}_{i,k} - \vec{p}'_{j,0})}{\| \vec{p}_{i,k} - \vec{p}'_{j,0} \|^3},$$ (6)

214   and integer $k = 2 \dots K$ is the index of the electric field line at point $\vec{p}_{i,k}$, points $\vec{p}_{j,0}$ are the locations

215   of the contributing charges $\hat{q}_j$ on the inner boundary contour, points $\vec{p}'_{j,0}$ are the locations of the

216   contributing charges $\hat{q}'_j$ on the outer boundary contour (green points on Figure 2a), where $\hat{q}_j$ and $\hat{q}'_j$

217   are arbitrary positive and negative electric charges, respectively. This process is repeated until either

218   the electric field line reaches the opposite boundary, or a user-defined maximum number of steps

219   K_{max} has been reached. Whether the field line has reached the outer boundary is checked by verifying

220   if $\vec{p}_{i,k}$ lies within the annulus or on/beyond the outer boundary contour. Note that Equation (4) defines

221   a window of $2w + 1$ points on the inner and outer boundary contours that slides with the index i of

222   the respective field line. This selection includes neighbouring points confined within the boundary

223   contours, which are not necessarily the closest points to $\vec{p}_{i,k}$ in terms of in-plane Euclidean distance

224   as required by Equation (1). This might lead the algorithm to fail with 'stray' or 'collapsed' field lines

225   due to inaccurate approximation of the electric field, as discussed next. To improve the estimation,

226   one can increase w at the expense of computational time.

227   A beneficial bi-product of using electric fields for the definition of the internal contours is the control

228   it provides over the curvature of the electric field lines. This may be tuned via appropriate selection of

229   the relative amplitude of the charges on the boundaries of the tube, a parameter we may call 'rigidity'

230   (see Figure 2c-d). In practice, this is achieved by defining $\hat{q}_j = 1$ for all charges on the inner boundary

231   and $|\hat{q}'_j| = rigidity$ (user-defined positive, real value) for the charges on the outer boundary. This

232   essentially weights the contributions to the electric field defined in Equation (6), provided by the

233   charges on the outer boundary ($\hat{q}'_j$) vs. the contributions of the charges on the inner boundary ($\hat{q}_j$).

234   Tuning the rigidity results in straighter or more curved electric field lines, thus providing flexibility to

235   capture irregular tubular shapes that are heavily deformed (see Figure 2d).

236 The computational approach to iteratively approximate the electric field lines described above

237 reduces the computational cost to calculate the exact value of the electric field at all possible positions

238 in space, as per Equation (1). This approximation, involving a (i) discrete, user-defined electric field

239 line segment size δ for progressing through the annulus, (ii) a user-defined electric field search window

240 ($J = j \bmod I$, $j = i - w, \ldots, i, \ldots, i + w$, $w \in \mathbb{N}$) encompassing a limited number of contributing

241 charges, and (iii) manual tuning of the relative electric charge magnitudes or rigidity, might provide

242 'stray' or 'collapsed' electric field lines that do not reach the opposite boundary (see Figure 2a). Such

243 field lines are identified and removed as follows: Stray lines are defined/identified as exceedingly long

244 lines, and they are rejected by introducing a maximum number of iterations for the computation of

245 each electric field line: $K \leq K_{max}$. Collapsed field lines are defined as lines that do not progress far

246 from the initial point $\vec{p}_{i,0}$, and they are identified as the lines with variance V_i less than a user-defined

247 minimum electric field line variance V_{min}:

$$V_i = \frac{1}{K} \sum_{k=0}^{K} \left(\vec{p}_{i,k} - \overrightarrow{\overline{p_i}}\right)^T \left(\vec{p}_{i,k} - \overrightarrow{\overline{p_i}}\right), \tag{7}$$

248 where

$$\overrightarrow{\overline{p_i}} = \frac{1}{K} \sum_{k=0}^{K} \vec{p}_{i,k} . \tag{8}$$

249 Each electric field line i is then represented by a cubic spline fitted through all points $\vec{p}_{i,k}$ ($k = 0 \ldots K$).

250 Note that, once the electric field lines are transformed form a collection of points $\vec{p}_{i,k}$ to cubic splines,

251 the notation $\vec{p}_{i,k}$ is hence abandoned and the cubic splines are resampled as follows: Firstly, the local

252 thickness d_i at $\vec{p}_i$ is defined as the length (in number of pixels) of the electric field line i. Internal

253 contours are then created at a total of C (user-defined) depth levels at incremental percentages

254 (0%-100%) of each individual electric field line's length d_i (see Figure 2b): Relative depth levels are

255 defined as $\frac{c}{C-1} \cdot 100\%$ and absolute depth levels as $\frac{c}{C-1} \cdot d_i$ ($c = 0,1, \ldots, C - 1$) with c, C being positive

256 integers. Explicitly, for $C = 3$: $\frac{0}{2} \cdot 100\% = 0\%$ (inner boundary), $\frac{1}{2} \cdot 100\% = 50\%$, $\frac{2}{2} \cdot 100\% = 100\%$ (outer

257 boundary). See Figure 2b for an example of four (C = 4) different relative depth levels (0%, 33%, 67%,

258 100%). The number of relative depth levels C determines the number of equidistant, non-overlapping

259   contours (including the internal boundary at 0% and the external boundary at 100% relative depth

260   level), which can be chosen arbitrarily. Each contour $cont_{h,c}$ is defined by fitting a cubic (in-plane)

261   spline at height level h through all points on the electric field lines i that correspond to depth level c

262   or absolute depth levels $\frac{c}{C-1} \cdot d_i$. As some of the electric field lines may have been discarded (stray or

263   collapsed field lines) the resulting internal contours might consist of fewer points than the boundary

264   contours. To obtain a uniform representation, each cubic spline representing one specific contour

265      $cont_{h,c}$ is resampled with a total of I samples.

266   As the approximation of the electric field lines is the most computationally intensive part of our

267   method to generate 3D cycloramas, it is only applied on every m^{th} slice or 2D section of the 3D image

268   stack (positive integer m: interpolation interval) that depicts the deformed tube, resulting in contours

269      $cont_{h,c}$ on sections $sect_h$ ($h = 0, m, 2m, …$ and $h \leq H - 1$ with H the total number of slices) at depth

270   level c as shown in Figure 2e. To generate the contours $cont_{h,c}$ on the remaining sections $sect_h$ ($h \neq$

271      $0, m, 2m, …$), the contours of the selected 2D cross sections are then interpolated across all sections

272   of the 3D image stack. In detail, vertical cubic splines are fitted on corresponding points, i.e., the ith

273   spline is created by selecting the ith point on each contour for each depth level c (see Figure 2e).

274   Eventually $cont_{h,c}$ is defined as the set of all points at cross section h and depth level c: $cont_{h,c} =$

275      $\{\vec{p}_{i,h,c}\}$.

276   Once contours have been defined at all depth levels c and for all 2D cross sections h, each 3D re-slicing

277   or an onion-like surface at relative depth level $\frac{c}{C-1} \cdot 100\%$ is defined as the set of all 2D contours at

278   depth level c. The basic components are then ready to generate internal 2D panoramic views of the

279   deformed cylindrical sample and 3D cycloramas as explained in the next section. At this point, the

280   problem of volumetric unrolling of deformed tubes has been reduced to the simpler and already

281   solved problem of manifold embedding or mapping 3D surfaces onto 2D equivalents as discussed next.

2.3. Mapping: Generation of 3D cycloramas

To generate 2D panoramic views at different relative depth levels $\frac{c}{C-1} \cdot 100\%$ of the deformed tube, the 3D re-slicing surfaces need to be mapped onto 2D equivalents (2D cycloramas). The problem has been widely studied in the literature, and several interesting approaches are discussed in section '4. Discussion'. Here, we adopt a simple and basic approach as a proof-of-concept. Mapping is performed on a contour-by-contour basis, where the boundary and internal contours need to be mapped onto rectangular grids. When stacked together, these 2D panoramic views become a 3D cyclorama, which displays the boundaries and particularly the internal structure of the sample at different depth levels (see Figure 3).
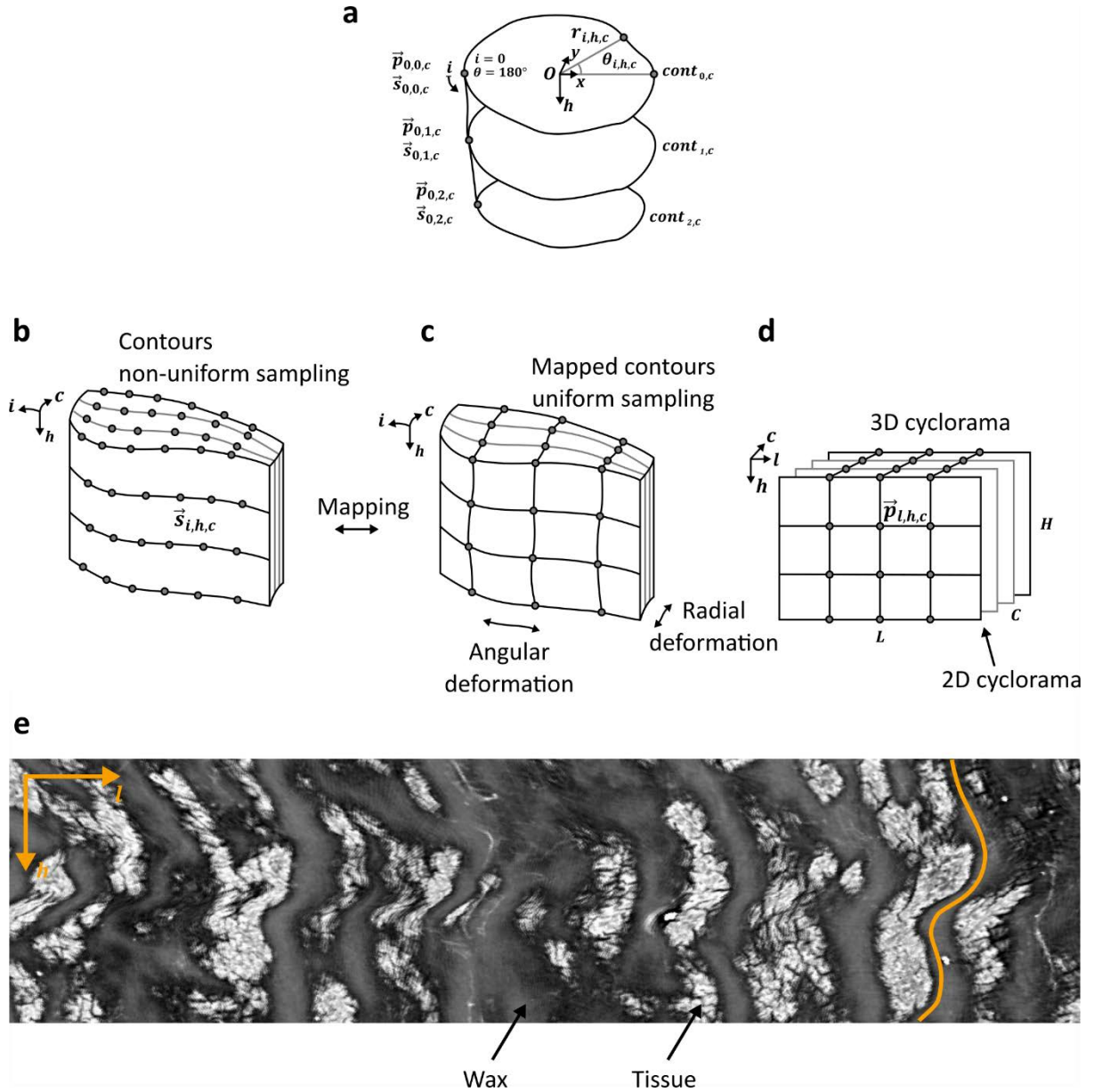
Figure 3: Linear mapping of 3D re-slicing surfaces

(a) The re-slicing surface edge at depth level c is defined by selecting the first point $\vec{s}_{i,h,c} = \vec{s}_{0,h,c} = (r_{0,h,c}, 180°)$. (b) Initial re-slicing surfaces are represented as unstructured contours. (c) The points in the unstructured contours in b are mapped onto the structured grid in c. (d) The structured grid shown in c is used to probe the 3D image data and create the 3D cyclorama. (e) A section of a 2D cyclorama at 0% relative depth level ($c = 0$: inner boundary) of a healthy murine colon embedded in paraffin wax, which partially probes volumes from the background (paraffin wax) and the sample (tissue). Vertically curved patterns are visible, as revealed by the orange outline of the tissue. This is a

300   consequence of local image deformations (stretching/contraction), which results in anisotropic pixel

301   sizes.

302   Initially, the length of all 2D panoramic views or 2D cycloramas is fixed at reference length L, defined

303   by the longest contour in the volume: $L := \max_{h=0\ldots H-1} \left(\max_{c=0\ldots C-1} L_{h,c} \right)$, with integer $L_{h,c}$ being the length

304   of contour $cont_{h,c}$ of section $sect_h$ at relative depth level c (see Figure 2e and Figure 3b) in number

305   of pixels (see Figure 3d). The longest contour thus defines the length L of the 3D cyclorama, while all

306   other contours ($L_{h,c} \leq L$) are dilated to match up with the longest contour. On this account, the

307   resulting (non-uniform) pixel size of the 3D cyclorama will be equal (for the longest contour) or larger

308   (all other contours) when compared to the pixel size of the original image data.

309   We then open the closed contours into sequences, by resampling each of the contour splines so that

310   contour $cont_{h,c}$ is (densely) represented by a total of $L_{h,c}$ points. Then, the first point $\vec{p}_{0,h,c}$ (point

311   with index $i = 0$), is arbitrarily but consistently selected across all contours $cont_{h,c}$ as follows (see

312   Figure 3a): We can express the points of each contour $cont_{h,c}$ that are initially defined in Cartesian

313   coordinates $\vec{p}_{i,h,c} = (p_{i,h,c_x}, p_{i,h,c_y})$ in polar coordinates:

$$\vec{s}_{i,h,c} = \left(r_{i,h,c}, \theta_{i,h,c} \right), \quad i = 0 \ldots L_{h,c} - 1 , \tag{9}$$

314   with $O = (o_x, o_y)$ an arbitrary rotation axis inside the tube, $r_{i,h,c}$ the Euclidean distance from the

315   rotation axis, and $\theta_{i,h,c} \in [0 \ldots 2\pi)$ the azimuthal angle in radians. The first point $\vec{p}_{0,h,c}$ or $\vec{s}_{0,h,c}$ is

316   chosen as the point among all points on contour $cont_{h,c}$ with $\theta_{i,h,c}$ closest to π radians or 180 degrees

317   (see Figure 3a).

318   Mapping of the boundaries and internal contours onto 2D cycloramas or 2D panoramic views (with a

319   fixed length L) is performed by uniformly sampling each boundary and internal contour with the same

320   number of points as the longest/reference contour (see Figure 3c). In other words, all contours except

321   from the longest/reference contour are resampled once again, so that contour $cont_{h,c}$ is represented

322   by a total of L points, effectively stretching each contour to fit the longest contour in the volume. This

19

323   'linear' mapping avoids collapsing of points and contraction. It results in a uniform pixel size along

324   individual lines (horizontal or l-dimension in Figure 3e) of the cyclorama image but not necessarily the

325   same pixel size across all lines (vertical or h-dimension in Figure 3e), as each contour is stretched

326   individually. This effectively spreads the image deformation across the entire image, resulting in wavy

327   but continuous cycloramas as shown in Figure 3e. Note that any mapping approach tries to spread the

328   inevitable image deformation throughout the image, typically by applying a mapping that is optimal

329   in some respect. Alternative approaches are discussed in section '4. Discussion'. The mapping process

330   we implemented defines which index i corresponds to each index l in the stretched contour as follows:

$$i \leftrightarrow l, \ i \in \left\{ 0 \dots L_{h,c} - 1 \right\}, \ l = 0 \dots L - 1 \ . \tag{10}$$

331   These indices are then used to redefine the contours by selecting the points $\vec{s}_{i,h,c}$ that correspond to

332   each point $\vec{p}_{l,h,c} = (l, h, c)$ in the 3D cyclorama (see Figure 3b-d). The mapping between the 3D

333   surface, defined by all points with fixed depth level $\check{c}$, onto points on the 2D cyclorama plane is then

334   defined as:

$$\vec{s}_{i,h,\check{c}} \leftrightarrow \vec{p}_{l,h,\check{c}} \ . \tag{11}$$

335   One (planar) 2D cyclorama per depth level $\check{c}$ is created by probing the 3D image data volume at all

336   points $\vec{s}_{i,h,\check{c}}$ (see Figure 3b-d). Note that all 2D cycloramas, which correspond to a specific relative

337   depth level, are of equal size (equal length and height). This allows to create a stack of 2D cycloramas

338   from 0% (internal boundary) to 100% (external boundary) of the tube's relative depth level (3D

339   cyclorama), which is essentially an unrolled version of the deformed tube. This digital unrolling (onto

340   a 3D cyclorama) has been achieved by introducing image deformations in two directions: Radially,

341   through the definition of the relative depth levels using the electric field lines, and angularly, by

342   stretching and contracting the contours (see Figure 3c).

3. Validation of the 3D cyclorama method

Here we test the utility of our method for the study of crypt budding in early-stage CRC. We employ a well-established mouse model, and prepare cylindrical formalin-fixed paraffin-embedded (FFPE) colon samples with early-stage CRC. A sample preparation method is employed, where the original tubular shape of the colons is preserved. We then apply non-destructive 3D imaging using X-ray phase-contrast µCT, followed by digital unrolling using our 3D cyclorama method. This allows us to easily identify crypt budding in the 3D cycloramas and perform image segmentation of the budding crypts on the µCT data, where the original shape and orientation of the crypts is preserved. This approach allows for accurate quantification of the 3D shape of the crypts using µCT and subsequent functional studies using traditional paraffin sectioning and histology methods.

3.1. Validation methods

Animal model

An azoxymethane and dextran sodium sulphate (AOM/DSS) mouse model was used to produce a murine colon sample with early stage colorectal cancer. The model uses AOM, which is a procarcinogen that inflicts DNA damage before it is excreted into the bile and taken up by the colonic epithelium [38], and DSS, which is a polysaccharide that inflicts epithelial damage in the colon and inflammatory response [39]. The specific protocol applied here was adapted from Neufert *et al.* [40] and Parang *et al.* [41] as follows: A C57BL/6J male mouse that was 8 weeks old at the beginning of the experiment was treated with one intra peritoneal injection of 10 mg/kg AOM solution on day 1. Next, starting on day 3, the mouse was treated with 2 % weight/volume DSS solution in sterile water for 7 days, followed by 14 days of sterile water provided *ad libitum*, via a mouse water drinking bottle (inflammation and healing phases, respectively). One healthy (untreated) and one AOM/DSS-treated mouse were culled via schedule 1 on day 24 and the distal colons were excised. In order to preserve the original shape of the colonic tissue, the lumen was filled with fixative before the two ends were sealed with sutures. The resulting sample looks like a 'sausage' [13]. The samples were fixed in 10 %

368 neutral buffered formaldehyde for 2 days, before 10 mm-long tubular pieces were embedded in

369 paraffin wax using a plastic drinking straw as a mould to create cylindrical paraffin wax blocks.

370 The animals were bred and maintained in the Biomedical Research Facility, University of

371 Southampton, Southampton, UK, in accordance with the United Kingdom Animals (Scientific

372 Procedures) Act 1986. This study has received ethical approval from the Animal Welfare and Ethical

373 Review Body (AWERB) of the University of Southampton, UK, and was operated under an existing

374 Home Office animal (scientific) procedures project licence. The regulatory protocols were performed

375 according to the animal research reporting of in vivo experiments (ARRIVE) guidelines [42]. The animals

376 were kept at constant temperature of 22±2 °C with food and filtered water available *ad libitum* and

377 were killed under the Schedule 1 procedure.

378 **X-ray CT imaging**

379 Both samples were imaged using synchrotron light-based X-ray CT at beamline I13-2 of the Diamond

380 Light Source, Didcot, UK, at an energy of 25 keV, exposure time of 85 ms per X-ray projection for 2501

381 projections, an (isotropic) voxel size of 2.2 µm and an X-ray propagation distance (sample-to-detector

382 distance) of 230 mm. Phase retrieval was performed using the Paganin algorithm [43], prior to standard

383 filtered back projection (FBP) [14] for CT reconstruction using the in-house implementation (Savu version

384 2.2) [44]. From each of the resulting CT stacks (see Figure 4a), a subset of 301 reconstructed CT slices

385 (height of 0.66 mm) were extracted, each 1841×1841 pixels^2 or 4.1×4.1 mm^2 in size.
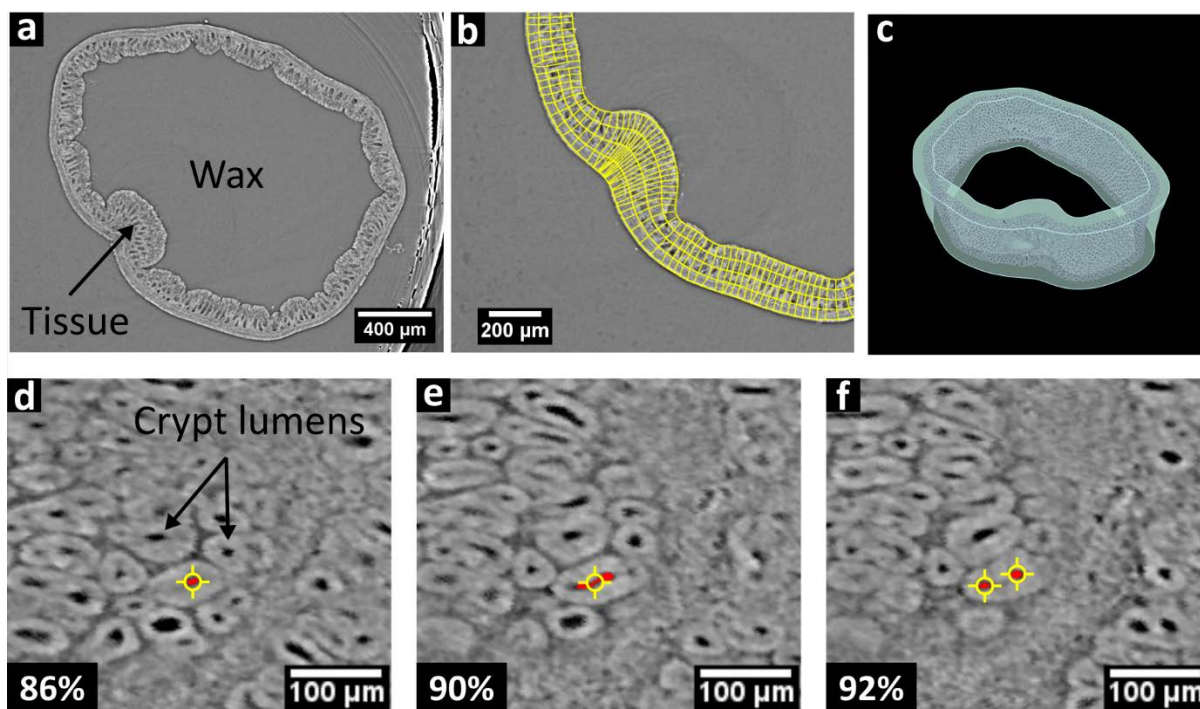
Figure 4: 3D cycloramas for the study of murine colons

(a-c) A healthy murine colon embedded in paraffin wax. (a) A SR CT section of the intact colon. (b) Virtual electric field lines and the resulting contours ($C = 5$ instead of the total $C = 30$ depth levels are shown here for visual clarity). (c) CT grey values are shown at 50% relative depth level, while boundary surfaces are shown transparent. (d-f) Unrolled CT stack of a murine colon with early stage colorectal cancer. The 3D cyclorama has a total of $C = 50$ slices or depth levels, where sequential slices at relative depth levels of 86%, 90% and 92% correspond to slices 42/49, 44/49 and 45/49, respectively. Crypt budding is revealed when a single colonic cross section, shown here in red, divides from one to several branches when moving from one slice to the next at a different colonic tissue depth, i.e. moving from e. to f. Yellow crosses show points created inside individual budding crypts on each cyclorama slice.

Image processing and visualisation

In order to digitally unroll the samples using our 3D cyclorama method the boundaries of their tubular volume were manually defined as follows: For the healthy sample all tissue layers were selected via manual definition of the boundary contours at the boundaries between the tissue and the paraffin

402 wax (see Figure 4a-b). For the sample of the AOM/DSS-treated mouse the mucosal layer was selected

403 via manual definition of the boundary contours, in order to isolate the crypts. Both samples were

404 unrolled with $I = 200$ point-long contours, electric field search windows of 31 points ($w = 15$),

405 electric field line segment sizes of $\delta = 2$ pixels, minimum electric field line variance $V_{min} = 50$, rigidity

406 equal to 1, interpolation interval $m = 20$ and rotation axis origin $O = (1080,780)$. For the healthy

407 sample a total of $C = 30$ depth levels and a maximum number of steps $K_{max} = 75$ were selected.

408 The resulting 3D cyclorama's length was $L = 2582$ pixels, the height $H = 301$ pixels, and the depth

409 $C = 30$ slices. For the AOM/DSS-treated sample a total of $C = 50$ depth levels and a maximum

410 number of steps $K_{max} = 50$ were selected for increased spatial resolution in the c-direction (see

411 Figure 2d). The resulting 3D cyclorama had a length of $L = 2530$ pixels, height $H = 301$ pixels, and

412 depth $C = 50$ slices. The unrolling process, including the processing and writing the results to disk,

413 took less than five minutes for each sample (laptop computer with Intel® Core™ i5-6300U @ 2.5GHz,

414 2 cores, 4 logical processors, and 16 GB of RAM).

415 We firstly identified crypt budding on the 3D cyclorama, and subsequently performed image

416 segmentation and quantification on the original 3D CT stack, and not on the reformed 3D cyclorama,

417 as follows: After unrolling, sequential slices of the 3D cyclorama depict cross sections of the crypts at

418 different depths of the colonic tissue. We traced individual crypts through the colonic tissue layers at

419 different depths, i.e. through individual layers of the 3D cyclorama. We then identified non-budding

420 crypts as those with a single cross section that did not divide on any of the cyclorama layers

421 representing different colonic tissue depths. Budding crypts were identified by pinpointing those

422 locations where a single colonic cross section divided from one to multiple cross sections. We then

423 manually created a point ('Point tool' in Fiji) inside each of the crypts on each cyclorama layer. Hence,

424 each crypt was represented by a set of points in 3D defined on the individual cyclorama layers (Figure

425 4d-f).

426   Next, we used ITK-SNAP (v2.8.0-beta) for isolation of the crypts in 3D. ITK SNAP [266]

427   (www.itksnap.org), an open-source image processing application to segment 3D structures in image

428   stacks, provides semi-automatic segmentation using active contour methods. It requires a (set of) seed

429   volumes that are expanded over the 3D image by applying a region growing algorithm. The iterative

430   region growing algorithm maintains a curve or active contour. The contour evolves under the influence

431   of a region completion force that tends to expand the curve, and a smoothing factor that tends to

432   make the curve less rugged. On each iteration, ITK-SNAP reads the image grey values around the curve

433   and decides how the curve needs to evolve in order to segment the crypts. We created the seed

434   volumes for ITK-SNAP as a binary mask with a zero value for the background, and cubes of $5\times5\times5$

435   pixels^3 (or $11\times11\times11$ μm^3) with a value equal to one, centred on each of the points (inside the crypts)

436   on the cyclorama. We subsequently mapped this cyclorama mask back onto the CT stack using the

437   inverse of the computed mapping between the CT stack and the 3D cyclorama, resulting in a (binary)

438   CT mask. The bit-depth of the CT stacks was reduced from 16 bit to 8 bit with grey-value clipping

439   thresholds at 21,000 a.u. and 37,000 a.u. (derived using the 'Auto-threshold tool' in Fiji, with the

440   default algorithm: 'isodata' [45]). The back-mapped seed volumes resulting from the inverse mapping

441   appear as red cubes in the 3D view, and as red overlaid areas on the orthogonal views of Figure 5a.

442   This 3D binary CT mask had the same dimensions as the CT stack of the colonic segment

443   ($1844\times1844\times301$ pixels^3 or $4.1\times4.1\times0.7$ mm^3), and was provided to ITK-SNAP as an initial image

444   segmentation. We then initialised the region growing algorithm with these seed volumes and ran it

445   for 200 iterations with a low-pass filter threshold of 117 a.u., a region completion force equal to 1,

446   and a smoothing factor of 0.2. Upon completion, the region growing algorithm provided a 3D

447   segmented stack composed of slices such as that shown in Figure 5b, a 3D volumetric reconstruction

448   of which is shown in Figure 5c.
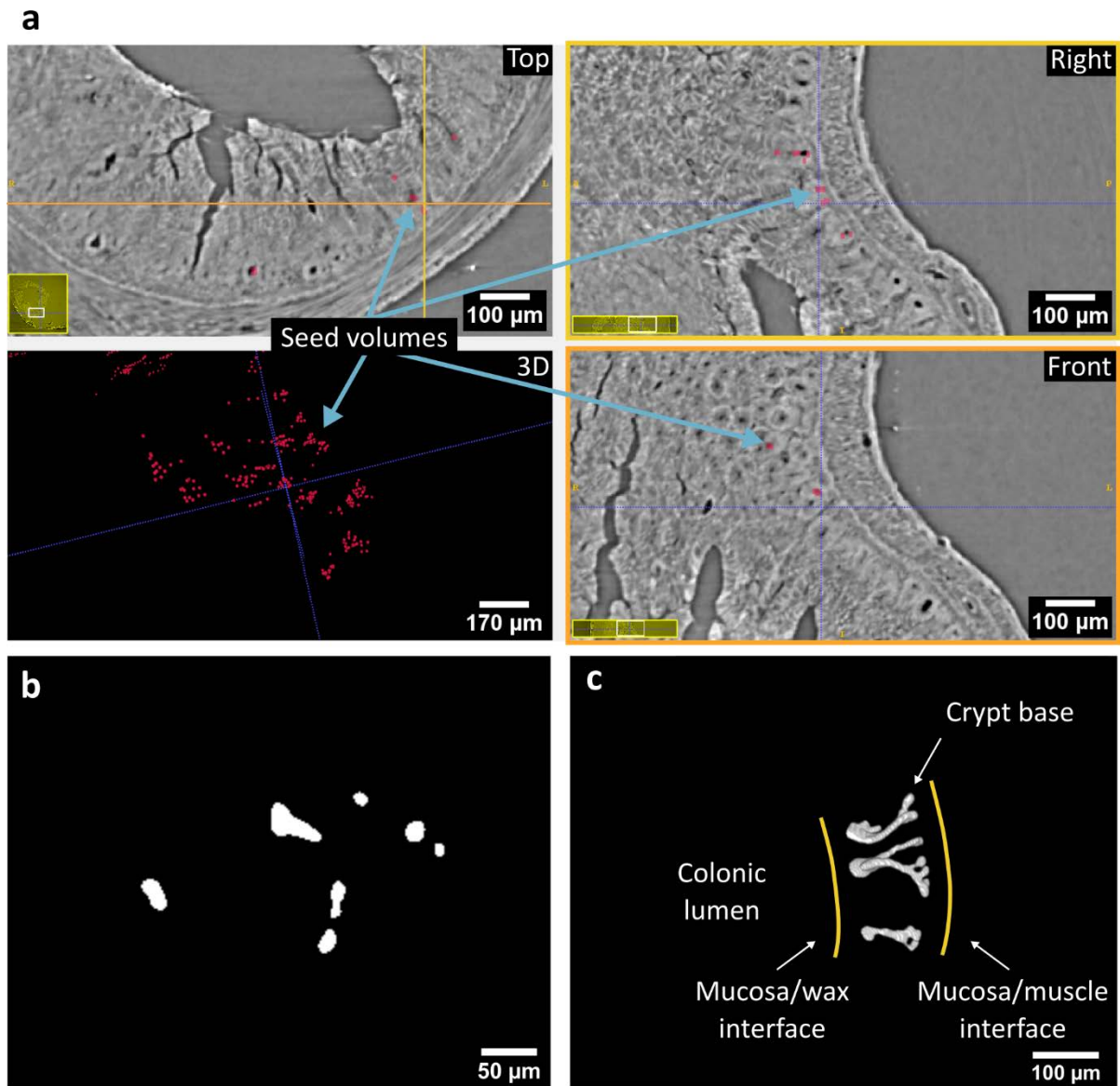
Figure 5: Budding crypt identification and 3D segmentation

(a) The viewport of ITK-SNAP is composed of four views (Top, Right, Front and 3D). The panels Top, Right and Front show orthogonal cross sections of the SR CT stack. The panels Right and Front show cross sections across the yellow and orange lines on the panel named Top, respectively. The panel named 3D shows the CT mask with the volumes of the back-mapped seed points (resulting from the inverse mapping between the 3D cyclorama and the CT data). The 3D seed volumes shown in the panel 3D, which are overlaid on the CT stack in the panels named Top, Right, and Front, are used to initialise the segmentation and expand it throughout the crypt lumens using region growing. The panels named Top, Right and Front only show a zoomed-in view of the respective orthogonal cross sections. The

459   white rectangles within the yellow panes on the bottom left corners of the Top, Right and Front panels

460   show which part of the cross sections is displayed in the panel. (b) Each slice of the image stack

461   produced by the segmentation procedure is a binary image, with pixels corresponding to the crypt

462   lumens having the value of one (white) and zero (black) elsewhere. (c) A 3D rendering of the binary

463   image stack reveals the budding crypts and their position in space within the tissue.

464   ## 3.2.   Validation results: Murine colon unrolling

465   The process of identifying budding crypts in the unrolled murine colons is shown in Figure 4. An

466   example of the electric field lines and contours (only $C = 5$ depth levels are shown here for visual

467   clarity) resulting after the application of virtual electrical charges on the colonic boundaries is shown

468   in Figure 4b. Figure 4c provides a photorealistic 3D rendering that illustrates the sample's boundaries

469   and the re-slicing surface at 50% relative depth level, yielding the probed CT greyscale values. Figure

470   4d-f show segments of the 2D cycloramas at the incremental relative depths (80%, 82%, 84%), which,

471   being locally perpendicular to the colonic crypts, depict the colonic crypts as circular profiles. For the

472   untreated sample, the healthy crypts do not split, and hence, their cross sections are consistent

473   throughout all cyclorama slices (see Supplementary video 1). The AOM/DSS-treated mouse, however,

474   exhibits crypt budding, which is readily visible in the 3D cyclorama by identifying the tissue depth

475   where a single crypt cross section splits to more than one (see Supplementary video 2).

476   Note that, not only the original shape of the crypts has been preserved in the cyclorama, but also their

477   relative location and orientation in space. This is only possible because, our method avoids physical

478   cutting, thus tissue distortions typical for conventional (2D) thin section-based histology [46] are not an

479   issue. Moreover, each of the 2D cycloramas representing internal tissue layers at a specific tissue

480   depth can be further analysed, for instance to count the number of crypts and their number density.

481   In other words, our 3D cyclorama method advances time-consuming traditional (2D) thin-section

482   histology via the use of re-slicing onion-like surfaces that follow the 3D shape of the colon, while

483   obtaining non-planar slices across the entire tissue block. This internal re-slicing is impossible in

484   standard (2D) thin-section histology due to the nature of the involved (planar) physical sectioning. This

485   capability provided by our method is the key enabling feature for the *in situ* study of crypt budding in

486   3D.

487   When it comes to computational models of crypt budding, they have been confined to the study of

488   the healthy case of crypt fission. This is partly because validation of mathematical models of the crypt

489   is particularly difficult, either due to the lack of experimental data or the difficulty to measure certain

490   model parameters [47,48]. Notably, recent studies of crypt budding relate the spatial concentration of

491   proteins (including the APC, β-catenin, E-cadherin and survivin) and cell proliferation and

492   differentiation (including stem and mucus-secreting cells) with the crypt budding process [49-51]. By

493   employing non-destructive CT imaging of intact FFPE colon samples, our method facilitates a

494   correlative approach where concurrent structural information (via CT) and functional information (via

495   serial histology sections) is now possible, whereby for the first time *in situ*, 3D, structural and

496   functional characterisation of crypt budding during the early stages of CRC can be performed.

4. Discussion

Today, application areas of μCT and SR CT are broad, including archaeology, biology, chemistry, environmental science, forensics, material science or physics [14,52]. To physically unroll samples is often impossible or destructive [25]. On this account, non-destructive 3D imaging, such as confocal laser scanning microscopy, magnetic resonance imaging or X-ray computed tomography, and subsequent digital unrolling is an alternative method to study the sample's 3D structure. A method for digital unrolling of deformed tubes would be beneficial for a broad spectrum of scientific and industrial applications.

In the field of archaeology deciphering of ancient scrolls [25-28] or studying the wrapping material of mummified cats [53] are prime examples where digital unrolling is beneficial and has been used in the past. Inscriptions on metallic scrolls (lead, silver, gold or alloys), though, extend over a certain depth within the metal [54]. As a result, existing approaches to unroll these samples are only applicable to relatively thin samples with close to uniform thickness. Hence, such cases could benefit from a volumetric unrolling approach, such as our method, to extract the full 3D nature of the inscribed literals. Similarly, in industry, procedures for non-destructive testing of turbine blades or aircraft wings, which are examined for fatigue life faults and internal microcracks during manufacture and/or maintenance [52,55,56], could also be facilitated by our 3D cyclorama. Unrolling or flattening manufactured parts with challenging geometries could speed-up the examination for 3D crack propagation and manufacturing defect distribution via effective visualisation of the sample's volume.

Our 3D cyclorama method can facilitate visualising the internal structure of deformed cylindrical tubes of non-uniform thickness, yet the projected volumes should be interpreted with care. The 3D cyclorama is deformed in both angular and radial directions, thus the scale is not preserved, resulting in anisotropic and non-uniform pixel/voxel sizes. This uneven scale implies that distances should not be measured on cycloramas. Nevertheless, the sample topology is always preserved, i.e., neighbouring features in the original volume will always remain neighbours in the projected space (i.e., cycloramas)

522   and *vice versa*. This originates in the construction of the re-slicing surfaces and the mapping, whereby

523   we create the re-slicing surfaces based on (virtual) electric field lines that never overlap. We further

524   make use of a mapping approach that offers two benefits. First, contours are mapped independent of

525   each other, allowing implementation of the algorithm in a multi-threaded fashion to improve

526   computational performance. Secondly, it creates cycloramas identical in size and shape, readily solving

527   the subsequent registration problem, i.e., the problem of aligning 2D cycloramas from different

528   depths of the tube, so that features extending over several layers match up and are represented as

529   continuous entities within the 3D cyclorama. This unavoidably introduces image deformations across

530   the entire image, resulting in wavy but continuous cycloramas as shown in Figure 3e.

531   It is worth to investigate the possibility of employing alternative mapping strategies not addressed

532   yet. Notably, as our approach treats each contour individually for the benefit of multithreading, this

533   confines our abilities to impose certain properties on the 2D cycloramas that result from the mapping,

534   such as minimal image deformation, maximal smoothness, etc. Approaches within the context of

535   manifold embedding could be used to impose such desired properties for the mapping of the 3D re-

536   slicing surfaces. Such methods are studied in the field of differential geometry [57], where manifolds

537   (topological spaces that are locally Euclidean) can be embedded in lower-dimensional equivalents.

538   In our case, the dimensionality of the re-slicing surface needs to be reduced from 3D to 2D. This

539   mapping (or embedding) can be done in different ways, including the isometric mapping [58] for minimal

540   image deformation, or the moving least squares mapping [59] for maximal smoothness, depending on

541   the desired properties of the target space. For instance, isometric mapping [58] computes the

542   embedding that optimally preserves geodesic distances between the points on the manifold. This

543   algorithm would preserve the shapes of features on the re-slicing surface, effectively minimising image

544   deformation of feature shapes on the mapped space. However, it would not ensure consistency

545   among the shape of all 2D equivalents since it does not necessarily yield rectangular images. This

546   means that each 3D re-slicing surface would be mapped onto a 2D equivalent with different

547   dimensions and shape. Hence, a subsequent step of registration among the 2D equivalents would be

548   necessary to match up features in sequential 2D surfaces to combine them into a 3D stack depicting

549   the unrolled volume. Our approach solves this problem by imposing identical shape and size for 2D

550   cycloramas that are stacked to produce a 3D cyclorama, at the expense of the image deformation

551   types discussed in section '2.3. Mapping: Generation of 3D cycloramas'.

552   The moving least squares approach [59] computes a mapping that yields a mapped surface with maximal

553   smoothness. This method requires the user to provide a small set of control point pairs (a point on the

554   source surface and its mapped position) and creates a smooth surface that respects the given set. This

555   method would be suitable to create rectangular 2D surfaces of identical size and shape. It is an elegant

556   and mathematically sound method that is worth investigation and integration with our approach of

557   reforming the deformed tube into onion-like re-slicing surfaces using electrostatics: The requirement

558   of a set of input control point pairs in the formulation of the moving least squares approach could be

559   conveniently integrated with the 3D cyclorama method given our definition of re-slicing surfaces as a

560   set of contours made up of sequences of points. Control point pairs could be created by matching up

561   points $\vec{s}_{i,hc}$ from the re-slicing surface (Figure 3b) with points $\vec{p}_{i,h,c}$ on the 3D cyclorama grid (Figure

562   3d). Selecting a small set of control point pairs would provide enough flexibility for image deformation

563   in both directions h and l (see Figure 3d-e) in addition to the radial image deformation (direction c)

564   already introduced through the definition of the relative depth levels (see Figure 3b-d). This flexibility

565   of image deformation in all directions would result in a smooth 3D image deformation field.

566   Although our current implementation for 3D cycloramas was developed to unroll deformed tubes, the

567   mathematical framework can, in principle, be applied to digital volume flattening/straightening of

568   thick sheets and scrolls of non-uniform thickness as well. To achieve this, the two boundary contours

569   would need to be open (non-convex), following the shape of the sheet/scroll. Adaptation of our

570   method to unroll scrolls of non-uniform thickness would advance the solution of digital unrolling of

571   ancient papyri and amulets with written or inscribed text [25-28], from a 2D approach to a fully 3D volume

572   unrolling, revealing information hidden in deeper layers of a scroll.

5.   Conclusion

573

574 We developed a method (3D cyclorama) to non-rigidly unroll deformed tubes of non-uniform

575 thickness. Virtual electrical charges were applied on the tube's boundaries, and by deriving the

576 resulting (virtual) electric field lines, we could generate internal onion-like 3D surfaces that followed

577 the shape of the deformed tube. This approach of using electrostatics to restructure a volume as

578 internal re-slicing surfaces is our main contribution to the problem of volume unrolling. We showcased

579 the utility of our 3D cyclorama method (validated) through application of digital unrolling of intact

580 colons for the study of crypt budding, and two case studies in Supplementary S.2 and S.3

581 (segmentation of microvilli in the human placenta and digital flattening of a 3D-printed adhesive film,

582 respectively), which present how our 3D cyclorama method can be applied to volumes imaged by

583 dissimilar 3D imaging techniques.

584 Applications of our method, however, go further beyond the case studies we presented here. It can

585 be useful for the analysis of digital volumes created by any 3D imaging technique, such as clinical CT,

586 confocal laser scanning microscopy, electron tomography, light sheet microscopy, magnetic

587 resonance imaging, X-ray CT, etc., with applications spanning a large range of fields, from archaeology

588 with unrolling of ancient scrolls and mummified cats to biomedical research, where abnormal crypts

589 are studied to better understand colorectal cancer.

Data and software availability

The data and software supporting this work are openly available from the University of Southampton institutional research repository at https://doi.org/10.5258/SOTON/D1407. The 3D cyclorama software developed through this work has been adapted as a Fiji plugin. The latest version of the plugin is made available through the Fiji update sites. For more information please visit https://imagej.github.io/plugins/3d-cyclorama.

Acknowledgements

Author contributions

C.R.: Conception, design, data acquisition, analysis and interpretation, software implementation and manuscript drafting. S.P.: Conception, data acquisition and interpretation, manuscript drafting and revision. P.S.: Conception, design, data analysis and interpretation, manuscript drafting and revision.

References

613 **References**

614 1   van Leeuwen, I. M. M., Byrne, H. M., Jensen, O. E. & King, J. R. Crypt dynamics and colorectal
615   cancer: advances in mathematical modelling. *Cell Proliferat* **39**, 157-181, doi:10.1111/j.1365-
616   2184.2006.00378.x (2006).

617 2   Wright, N. A. Epithelial stem cell repertoire in the gut: clues to the origin of cell lineages,
618   proliferative units and cancer. *Int J Exp Pathol* **81**, 117-143, doi:10.1046/j.1365-
619   2613.2000.00146.x (2000).

620 3   Totafurno, J., Bjerknes, M. & Cheng, H. The Crypt Cycle - Crypt and Villus Production in the
621   Adult Intestinal Epithelium. *Biophys J* **52**, 279-294, doi:10.1016/S0006-3495(87)83215-0
622   (1987).

623 4   Wasan, H. S. *et al.* APC in the regulation of intestinal crypt fission. *Journal of Pathology* **185**,
624   246-255 (1998).

625 5   Garcia, S. B., Park, H. S., Novelli, M. & Wright, N. A. Field cancerization clonality, and epithelial
626   stem cells: The spread of mutated clones in epithelial sheets. *Journal of Pathology* **187**, 61-81,
627   doi:10.1002/(Sici)1096-9896(199901)187:1<61::Aid-Path247>3.0.Co;2-I (1999).

628 6   Gupta, A. K. & Schoen, R. E. Aberrant crypt foci: are they intermediate endpoints of colon
629   carcinogenesis in humans? *Curr Opin Gastroen* **25**, 59-65,
630   doi:10.1097/MOG.0b013e32831db286 (2009).

631 7   Fujimitsu, Y. *et al.* Development of aberrant crypt foci involves a fission mechanism as
632   revealed by isolation of aberrant crypts. *Jpn J Cancer Res* **87**, 1199-1203, doi:10.1111/j.1349-
633   7006.1996.tb03133.x (1996).

634 8   Pretlow, T. P. *et al.* Aberrant Crypts - Putative Preneoplastic Foci in Human Colonic Mucosa.
635   *Cancer Res* **51**, 1564-1567 (1991).

636 9   Park, H. S. *et al.* Effects of epidermal growth factor and dimethylhydrazine on crypt size, cell
637   proliferation, and crypt fission in the rat colon. Cell proliferation and crypt fission are
638   controlled independently. *The American journal of pathology* **151**, 843-852 (1997).

639 10   Wargovich, M. J., Brown, V. R. & Morris, J. Aberrant crypt foci: the case for inclusion as a
640   biomarker for colon cancer. *Cancers (Basel)* **2**, 1705-1716, doi:10.3390/cancers2031705
641   (2010).

642 11   Erben, U. *et al.* Histomorphology of intestinal inflammation in inflammatory bowel diseases
643   (IBD) mouse models and its relevance for IBD in men. *Int J Clin Exp Patho* **9**, 408-442 (2016).

644 12   Shih, L. M. *et al.* Top-down morphogenesis of colorectal tumors. *P Natl Acad Sci USA* **98**, 2640-
645   2645, doi:10.1073/pnas.051629398 (2001).

646 13   Whittem, C. G., Williams, A. D. & Williams, C. S. Murine Colitis modeling using Dextran Sulfate
647   Sodium (DSS). *J Vis Exp*, doi:10.3791/1652 (2010).

648 14   Hsieh, J. *Computed Tomography - Principles, Design, Artifacts, and Recent Advances*. Third
649   edn, Vol. PM259 (Society of Photo-Optical Instrumentation Engineers (SPIE), Bellingham,
650   Washington, USA, 2015).

651 15   Thorsten, M. B. *Computed tomography: From photon statistics to modern cone-beam CT*.
652   (Springer, Verlag, Berlin, Heidelberg, 2008).

653 16   Katsamenis, O. L. *et al.* X-Ray Microcomputed Tomography for Nondestructive Three-
654   Dimensional X-Ray Histology. *The American journal of pathology* **189**, 1608-1620 (2019).

655 17   Newham, E. *et al.* Reptile-like physiology in Early Jurassic stem-mammals. *Nature
656   Communications* **11**, doi:10.1038/s41467-020-18898-4 (2020).

657 18   Newham, E. *et al.* Synchrotron radiation-based X-ray tomography reveals life history in
658   primate cementum incrementation. *Journal of the Royal Society Interface* **17**, 20200538
659   (2020).

660 19   Wittwer-Backofen, U., Gampe, J. & Vaupel, J. W. Tooth cementum annulation for age
661   estimation: Results from a large known-age validation study. *Am J Phys Anthropol* **123**, 119-
662   129, doi:10.1002/ajpa.10303 (2004).

663 20 Goggin, P. M., Zygalakis, K. C., Oreffo, R. O. C. & Schneider, P. High-resolution 3D imaging of
664   osteocytes and computational modelling in mechanobiology. *European Cells and Materials*
665   *(ECM)* **31**, 264-295, doi:10.22203/eCM.v031a18 (2016).
666 21 Goggin, P. *et al.* Development of protocols for the first serial block-face scanning electron
667   microscopy (SBF SEM) studies of bone tissue. *Bone* **131**, 115107,
668   doi:10.1016/j.bone.2019.115107 (2020).
669 22 Brown, M. S. & Seales, W. B. in *Proceedings Eighth IEEE International Conference on Computer*
670   *Vision (ICCV 2001).* 367-374 (IEEE).
671 23 Sun, M. X. *et al.* in *Tenth IEEE International Conference on Computer Vision (ICCV'05) Volume*
672   *1* Vol. 2 1117-1123 (2005).
673 24 Brown, M. S., Sun, M. X., Yang, R. G., Yun, L. & Seales, W. B. Restoring 2D content from
674   distorted documents. *IEEE Transactions on Pattern Analysis and Machine Intelligence* **29**,
675   1904-1916, doi:10.1109/Tpami.2007.1118 (2007).
676 25 Baum, D. *et al.* Revealing hidden text in rolled and folded papyri. *Applied Physics A* **123**, 171,
677   doi:10.1007/s00339-017-0808-6 (2017).
678 26 Bukreeva, I. *et al.* Virtual unrolling and deciphering of Herculaneum papyri by X-ray phase-
679   contrast tomography. *Scientific Reports* **6**, 1-7, doi:10.1038/srep27227 (2016).
680 27 Samko, O., Lai, Y. K., Marshall, D. & Rosin, P. L. Virtual unrolling and information recovery from
681   scanned scrolled historical documents. *Pattern Recogn* **47**, 248-259,
682   doi:10.1016/j.patcog.2013.06.015 (2014).
683 28 Allegra, D. *et al.* Virtual Unrolling Using X-Ray Computed Tomography. *Eur Signal Pr Conf*,
684   2864-2868 (2015).
685 29 Levy, B., Petitjean, S., Ray, N. & Maillot, J. Least squares conformal maps for automatic texture
686   atlas generation. *Acm T Graphic* **21**, 362-371 (2002).
687 30 Zhou, H. B. *et al.* Feature Guided Non-Rigid Image/Surface Deformation Via Moving Least
688   Squares with Manifold Regularization. *Ieee Int Con Multi*, 1063-1068 (2017).
689 31 Yu, C. *et al.* Image Deformation Using Modified Moving Least Squares with Outlines. *2017 Ieee*
690   *International Conference on Mechatronics and Automation (Icma)*, 1047-1051 (2017).
691 32 Wang, T.-H., Krishnamurti, R. & Shimada, K. Restructuring surface tessellation with irregular
692   boundary conditions. *Frontiers of Architectural Research* **3**, 337-347,
693   doi:10.1016/j.foar.2014.06.001 (2014).
694 33 Thiery, J. M., Tierny, J. & Boubekeur, T. Jacobians and Hessians of mean value coordinates for
695   closed triangular meshes. *Visual Comput* **30**, 981-995, doi:10.1007/s00371-013-0889-y (2014).
696 34 Schindelin, J. *et al.* Fiji: an open-source platform for biological-image analysis. *Nature Methods*
697   **9**, 676, doi:10.1038/nmeth.2019 (2012).
698 35 Schneider, C. A., Rasband, W. S. & Eliceiri, K. W. NIH Image to ImageJ: 25 years of image
699   analysis. *Nature Methods* **9**, 671, doi:10.1038/nmeth.2089 (2012).
700 36 Schindelin, J., Rueden, C. T., Hiner, M. C. & Eliceiri, K. W. The ImageJ ecosystem: An open
701   platform for biomedical image analysis. *Molecular reproduction and development* **82**, 518-529
702   (2015).
703 37 Griffiths, D. J. *Introduction to electrodynamics*. 4th edn, (Cambridge University Press,
704   Cambridge, UK, 2017).
705 38 Sohn, O. S., Fiala, E. S., Requeijo, S. P., Weisburger, J. H. & Gonzalez, F. J. Differential effects
706   of CYP2E1 status on the metabolic activation of the colon carcinogens azoxymethane and
707   methylazoxymethanol. *Cancer Res* **61**, 8435-8440 (2001).
708 39 Okayasu, I. *et al.* A Novel Method in the Induction of Reliable Experimental Acute and Chronic
709   Ulcerative-Colitis in Mice. *Gastroenterology* **98**, 694-702, doi:Doi 10.1016/0016-
710   5085(90)90290-H (1990).
711 40 Neufert, C., Becker, C. & Neurath, M. F. An inducible mouse model of colon carcinogenesis for
712   the analysis of sporadic and inflammation-driven tumor progression. *Nat Protoc* **2**, 1998-2004,
713   doi:10.1038/nprot.2007.279 (2007).

714 41 Parang, B., Barrett, C. W. & Williams, C. S. AOM/DSS model of colitis-associated cancer.
715   *Methods Mol Biol* **1422**, 297-307, doi:10.1007/978-1-4939-3603-8_26 (2016).
716 42 National Centre for the Replacement Refinement and Reduction of Animals in Research
717   (NC3R). *ARRIVE guidelines*, <https://www.nc3rs.org.uk/arrive-guidelines> (2021).
718 43 Paganin, D., Mayo, S. C., Gureyev, T. E., Miller, P. R. & Wilkins, S. W. Simultaneous phase and
719   amplitude extraction from a single defocused image of a homogeneous object. *Journal of*
720   *Microscopy* **206**, 33-40, doi:10.1046/j.1365-2818.2002.01010.x (2002).
721 44 Atwood, R. C., Bodey, A. J., Price, S. W. T., Basham, M. & Drakopoulos, M. A high-throughput
722   system for high-quality tomographic reconstruction of large datasets at Diamond Light Source.
723   *Philos T R Soc A* **373**, doi:10.1098/rsta.2014.0398 (2015).
724 45 Ridler, T. W. & Calvard, S. Picture Thresholding Using an Iterative Selection Method. *Ieee T*
725   *Syst Man Cyb* **8**, 630-632, doi:10.1109/tsmc.1978.4310039 (1978).
726 46 McInnes, E. Artefacts in histopathology. *Comparative Clinical Pathology* **13**, 100-108,
727   doi:10.1007/s00580-004-0532-4 (2005).
728 47 Almet, A. A., Maini, P. K., Moulton, D. E. & Byrne, H. M. Modeling perspectives on the intestinal
729   crypt, a canonical system for growth, mechanics, and remodeling. *Current Opinion in*
730   *Biomedical Engineering* **15**, 32-39, doi:10.1016/j.cobme.2019.12.012 (2020).
731 48 Tan, C. W., Hirokawa, Y., Gardiner, B. S., Smith, D. W. & Burgess, A. W. Colon Cryptogenesis:
732   Asymmetric Budding. *Plos One* **8**, e78519, doi:10.1371/journal.pone.0078519 (2013).
733 49 Boman, B. M. & Fields, J. Z. An APC:WNT Counter-Current-Like Mechanism Regulates Cell
734   Division Along the Human Colonic Crypt Axis: A Mechanism That Explains How APC Mutations
735   Induce Proliferative Abnormalities That Drive Colon Cancer Development. *Front Oncol* **3**, 244,
736   doi:10.3389/fonc.2013.00244 (2013).
737 50 Pin, C. *et al.* An individual based computational model of intestinal crypt fission and its
738   application to predicting unrestrictive growth of the intestinal epithelium. *Integrative Biology*
739   **7**, 213-228, doi:10.1039/c4ib00236a (2015).
740 51 Langlands, A. J. *et al.* Paneth Cell-Rich Regions Separated by a Cluster of Lgr5+Cells Initiate
741   Crypt Fission in the Intestinal Stem Cell Niche. *Plos Biol* **14**, e1002491,
742   doi:10.1371/journal.pbio.1002491 (2016).
743 52 De Chiffre, L., Carmignato, S., Kruth, J. P., Schmitt, R. & Weckenmann, A. Industrial applications
744   of computed tomography. *CIRP Annals* **63**, 655-677, doi:10.1016/j.cirp.2014.05.011 (2014).
745 53 Bewes, J. M. *et al.* Imaging ancient and mummified specimens: Dual-energy CT with effective
746   atomic number imaging of two ancient Egyptian cat mummies. *J Archaeol Sci-Rep* **8**, 173-177,
747   doi:10.1016/j.jasrep.2016.06.009 (2016).
748 54 Barfod, G. H., Larsen, J. M., Lichtenberger, A. & Raja, R. Revealing text in a complexly rolled
749   silver scroll from Jerash with computed tomography and advanced imaging software. *Scientific*
750   *reports* **5**, 1-10 (2015).
751 55 Wright, P., Fu, X., Sinclair, I. & Spearing, S. M. Ultra high resolution computed tomography of
752   damage in notched carbon fiber-epoxy composites. *J Compos Mater* **42**, 1993-2002,
753   doi:10.1177/0021998308092211 (2008).
754 56 Schilling, P. J., Karedla, B. P. R., Tatiparthi, A. K., Verges, M. A. & Herrington, P. D. X-ray
755   computed microtomography of internal damage in fiber reinforced polymer matrix
756   composites. *Compos Sci Technol* **65**, 2071-2078, doi:10.1016/j.compscitech.2005.05.014
757   (2005).
758 57 Spivak, M. *A comprehensive introduction to differential geometry*. 3rd edn, (Publish or perish,
759   INC., Houston, Texas, USA, 1999).
760 58 Tenenbaum, J. B., Silva, V. d. & Langford, J. C. A Global Geometric Framework for Nonlinear
761   Dimensionality Reduction. *Science* **290**, 2319-2323, doi:10.1126/science.290.5500.2319
762   (2000).
763 59 Schaefer, S., McPhail, T. & Warren, J. Image deformation using moving least squares. *Acm T*
764   *Graphic* **25**, 533-540, doi:10.1145/1141911.1141920 (2006).